ADVANCED MATERIALS INTERFACES
www.advmatinterfaces.de

Atomic Layer Deposition of the Conductive Delafossite $PtCoO_2$

*Dirk J. Hagen, Jiho Yoon, Haojie Zhang, Bodo Kalkofen, Mindaugas Silinskas, Felix Börrnert, Hyeon Han, and Stuart S. P. Parkin**

The first atomic layer deposition process for a ternary oxide is reported, which contains a metal of the platinum group, the delafossite $PtCoO_2$. The deposition with the precursors trimethyl-Pt-methylcyclopentadienyl, Co-bis(*N*-*t*-butyl-*N*′-ethylpropanimidamidate), and oxygen plasma results in a process with a nearly constant growth rate and stoichiometric composition over a wide temperature window from 100 to 320 °C. Annealing of the as-deposited amorphous films in an oxygen atmosphere in a temperature window from 700 to 800 °C leads to the formation of the delafossite phase. Very thin films show a pronounced preferred orientation with the Pt sheets being almost parallel to the substrate surface while arbitrary orientation is observed for thicker films. The conformal coating of narrow trenches highlights the potential of this atomic-layer-deposition process. Moreover, heterostructures with magnetic films are fabricated to demonstrate the potential of $PtCoO_2$ for spintronic applications.

1. Introduction

A considerable number of intriguing physical properties have been discovered in ternary and higher oxides containing metals of the platinum group during recent years. For example, the pyrochlore iridate $Y_2Ir_2O_7$ was one of the first proposed Weyl semimetals, although experimental investigations remained ambiguous. One reason for this is the difficulty of growing high-quality single-crystals, which is necessary for the direct proof of Weyl semimetallicity, e.g. by angle resolved photo-electron spectroscopy (ARPES).[1–9] The perovskites $SrIrO_3$ and $SrRuO_3$ were shown to exhibit a strong spin Hall effect[10,11] and to be effective materials for the shifting of magnetic domain walls by electrical currents,[12–14] respectively. Furthermore, the delafossites $PdCoO_2$ and $PtCoO_2$ turned out to be among the most conductive oxides. For example, Kushwaha et al.[15] determined a resistivity ρ as low as 2.1 μΩ cm at room temperature for $PtCoO_2$, the lowest value reported for an oxide thus far. Moreover, the conductivities reach values close to those of metals such as Cu, Ag, and Au at low temperatures.[15,16] These delafossites consist of two-dimensional Pd respectively Pt sheets connected by octahedrally coordinated CoO_2. Due to this structure, their electrical conductivity is strongly anisotropic and highest within the (ab) plane. Moreover, Kitamura et al.[17] predicted a large intrinsic spin Hall effect in $PtCoO_2$ from ab-initio calculations, which makes it an interesting material for spintronic devices such as ferromagnetic racetracks, in which the spin Hall effect is exploited for generating a spin current.[18–22]

Most of the work published thus far about these delafossites concerned bulk material. The deposition of $PdCoO_2$ thin films was only reported quite recently by Harada et al.[23] and Yordanov et al.[24] who used pulsed laser deposition (PLD) and by Brahlek et al.[25] who used molecular beam epitaxy (MBE). Harada et al.[23] needed a Pd-PdO target in addition to a $PdCoO_2$ target in order to obtain stoichiometric $PdCoO_2$ films at a growth temperature of 700 °C, while Brahlek et al.[25] carried out their MBE experiments at a growth temperature as low as 300 °C where they obtained amorphous films, which were crystallized by subsequent annealing. The low temperature was needed since other phases, Pd and Co_3O_4, were formed at higher temperatures. The loss of stoichiometry during PLD has also been observed for pyrochlore iridates. For example, Liu et al.[7] required a target with excess Ir for the deposition of $Y_2Ir_2O_7$. $PtCoO_2$ films have been grown by Wei et al.[26] using spin-coating of an aqueous solution and subsequent calcination at 750 °C in air. However, vacuum-based deposition techniques are usually preferred to spin-coating due to the better control of thickness and uniformity. Therefore, there is a demand for the development of alternative deposition methods for platinum metal containing oxides.

Atomic layer deposition (ALD) has been successfully implemented for the growth of a large number of ternary oxides.[27–40] For example, a review by Mackus et al.[41] from 2019 provides an extensive overview of ALD processes for ternary and higher oxides, as well as doped oxides. Interestingly, the authors list only one ALD process for such an oxide that contains a

D. J. Hagen, J. Yoon, H. Zhang, B. Kalkofen, M. Silinskas, F. Börrnert, H. Han, S. S. P. Parkin
Max Planck Institute of Microstructure Physics
Weinberg 2, 06120 Halle (Saale), Germany
E-mail: stuart.parkin@mpi-halle.mpg.de
D. J. Hagen
IHP GmbH–Innovations for High Performance Microelectronics
Im Technologiepark 25, 15236 Frankfurt (Oder), Germany
M. Silinskas
Technische Hochschule Wildau
Hochschulring 1, 25745 Wildau, Germany
The ORCID identification number(s) for the author(s) of this article can be found under https://doi.org/10.1002/admi.202200013.

DOI: 10.1002/admi.202200013

platinum group metal, Ru_xAlO_y. However, the reported material was rather a composite of metallic Ru and amorphous alumina than a ternary oxide phase.[42] We would like to mention that Minjauw et al.[43] reported ternary ALD processes for ruthenates during the preparation time for this article. This article focused on the low-temperature growth chemistry using RuO_4 with trimethyl aluminum and trimethyl-Pt-methylcyclopentadienyl ($Me_3Pt(CpMe)$) but did not report the formation of a crystalline ternary phase. One likely explanation for this lack of reported ALD processes is the difference of ALD processes for oxides of noble metals to those of non-noble metals. For noble metals, there is typically a competition between the growth of the pure metal and an oxide depending on the exact growth conditions. For example, Kim et al.[44] observed a shift from the growth of Ir to IrO_2 in an ALD process involving (ethylcyclopentadienyl) (1,5-cyclooctadiene)iridium and an Ar/O_2 mixture at 290 °C when the O_2 content in the Ar/O_2 mixture exceeded 75%. The transition pressure shifted to lower O_2 concentrations when the temperature was decreased. Hämäläinen et al.[45] reported a transition from the growth of metallic Pt to PtO_x in a process involving Pt-bis(acetylacetonate) ($Pt(acac)_2$) and O_3 when the deposition was carried out at temperatures below 140 °C. Knoops et al.[46] were able to deposit PtO_x in a much wider temperature window of 100–300 °C using $Me_3Pt(CpMe)$)and O_2 plasma when long plasma exposures were used. From shorter plasma exposures, metallic Pt was obtained at substrate temperatures above 200 °C. Hence, the important questions are: can the platinum group metal be deposited in an oxidized state in a ternary ALD process, and has the second metal any impact on this issue.

In this work, we approach this problem for the example of $PtCoO_2$ as for both Pt/PtO_x and CoO_x well-established ALD processes exist.[28,29,47–51] We first investigate the ALD of $PtCoO_2$ thoroughly using $Me_3Pt(CpMe)$, Co-bis(N-t-butyl-N′-ethylpropanimidamidate) (Co-AMD), and O_2 plasma, which is generated by a remote inductively-coupled-plasma (ICP) source. We have chosen these precursors because we used them in earlier work for the deposition of Pt, CoO_x, and Co-P.[52] Next, we explore the formation of the delafossite phase by annealing in different atmospheres and analyze the crystal structure. Finally, we investigate the suitability of $PtCoO_2$ for spintronic applications and the possibility to coat three-dimensional structures conformally.

2. Results and Discussion

2.1. Film Growth

As discussed above, the growth of PtO_x instead of Pt was observed in literature when the deposition temperature was lowered and when the oxygen exposure was increased. We, therefore, investigated if PtO_x can be grown at a low substrate temperature of 120 °C, and observed a transition from the growth of Pt to PtO_x when the pressure during the oxygen plasma exposure was reduced from 100 to 20 mTorr. This can be explained by the higher density of reactive species above the substrate when the ICP is generated at a lower pressure.[53,54] Therefore, we choose this temperature for the investigation of the ternary $PtCoO_2$ process by varying the growth parameters and measuring thickness and composition. Similarly to the binary process, the pressure during the oxygen-plasma exposure was a critical value as $PtCoO_2$ films could be readily obtained at a pressure of 50 mTorr and below with a growth per cycle (GPC) of about 0.7 Å while GPC and Pt concentration decreased significantly for 100 mTorr and further for 200 mTorr, where the films contained very little Pt (**Figure 1**d). Apparently, the influence of the pressure on the PtO_x part-process is much bigger than on the CoO_x part-process. Interestingly, the impact of the plasma power was much less significant as a noticeable decrease of the GPC was only observed for very low powers (25 W) (Figure S1, Supporting Information). The plasma-exposure time for the process to reach saturation was 4 s (Figure 1c). The strong plasma conditions made it very difficult to avoid a parasitic chemical-vapor-deposition (CVD) component during the CoO_x sub-cycle, and we had to modify the purging conditions (15 s purge after Co-AMD exposure, 20 s purge after plasma exposure, pressure-control valve completely open, plasma exposure 10 s) to ensure saturation during the pulse with the oxygen sensitive Co-AMD (Figure 1b). In contrast, the growth saturated after about 1s exposure of $Me_3PtCpMe$ (Figure 1a). The contrasting behavior of the two part-processes highlights the difficulty of the ALD of ternary oxides containing two dissimilar metals. We then used 20 mTorr plasma pressure for investigating how growth rate and composition change with the substrate temperature. As can be seen in Figure 1e, both remain nearly constant within the investigated temperature window from 100 to 320 °C, which is remarkable given the limited stability of Pt oxides. Furthermore, we demonstrated that the composition changes steadily with the ratio of the Pt and Co subcycles (Figure 1f).

Next, we deposited a thicker film (60 nm) in order to investigate composition and morphology more thoroughly. As can be seen from the X-ray photoelectron spectroscopy (XPS) depth profile in Figure S5, Supporting Information, the composition is very close to the stoichiometry $PtCoO_2$ nearly throughout the whole profile. X-ray diffraction (XRD) as well as transmission electron microscopy (TEM) showed that the film is amorphous (Figure 3a and Figure S7, Supporting Information). Furthermore, no indications for separated PtO_x-rich and CoO_x-rich phases could be observed. The determination of the chemical states of the elements from the high-resolution XPS scans is rather challenging. First, the Co 2p signals for the various oxides are very similar, so it is not possible to discriminate between a Co(III), Co(II), or mixed state from our data (Figure S4, Supporting Information). Second, the XPS signals are strongly dominated by the surface region and thus by potential post-deposition reactions in the atmosphere and by the final ALD step, which is oxygen plasma exposure. The Pt $4f_{7/2}$ and $4f_{5/2}$ peaks of the as-deposited film are quite sharp and centered at 74.3 and 77.6 eV, respectively (Figure S3, Supporting Information). Thus, they are between the literature values for PtO and PtO_2, respectively.[55] After sputtering, the spectrum broadens, showing the coexistence of different oxides with the lowest $4f_{7/2}$ signal at 72.2 eV, which is consistent with Pt(I) in $PtCoO_2$.

Finally, we investigated the suitability of our ALD process for coating three-dimensional structures. **Figure 2** shows

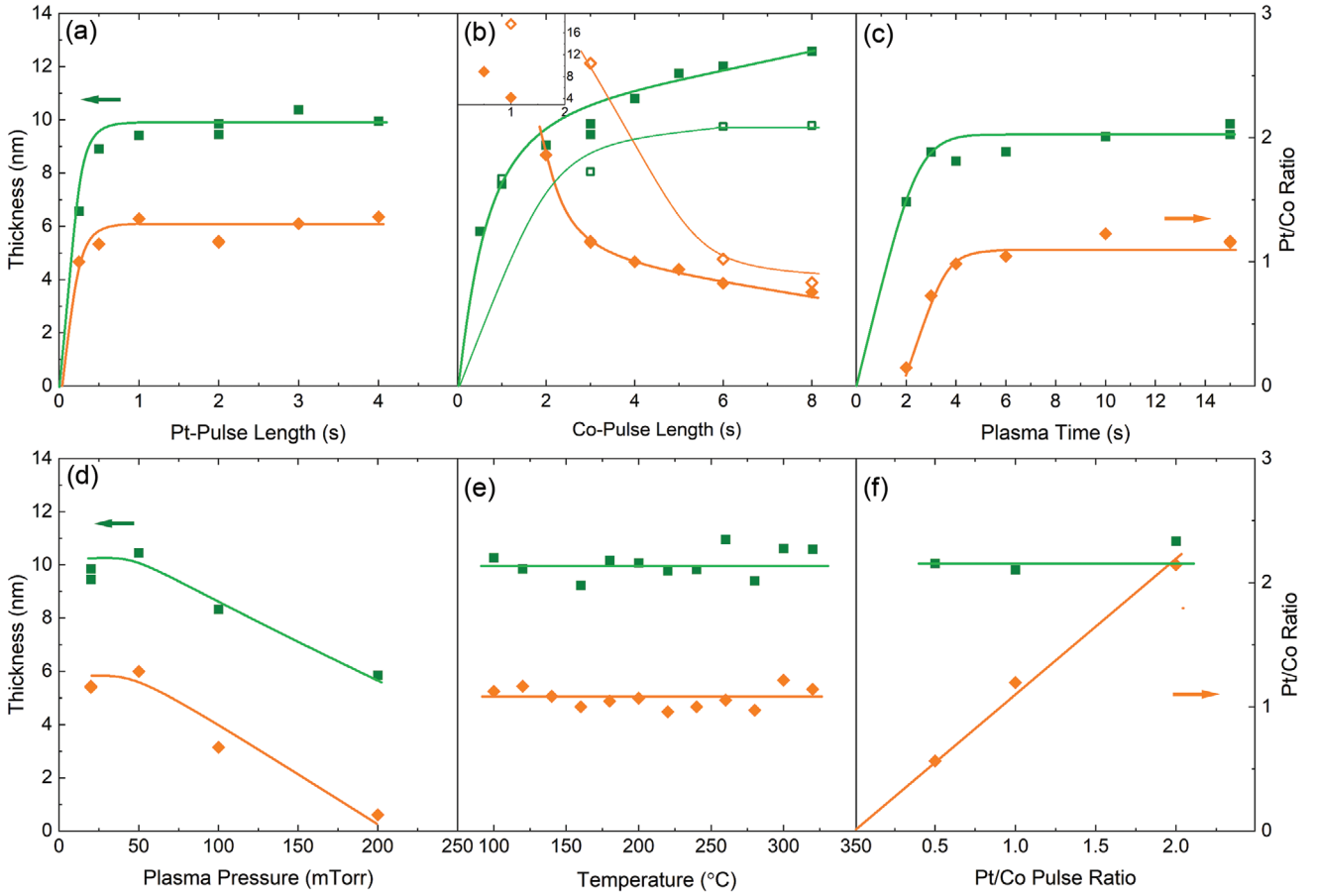

Figure 1. Characterization of the $PtCoO_2$ ALD process; thickness and composition versus duration of a) $Me_3Pt(CpMe)$, b) Co-AMD (the open symbols are for the process with longer purges; the inset is an extended right y-axis), and c) oxygen plasma exposure; d) versus pressure during plasma exposure; e) versus temperature; f) versus $Me_3Pt(CpMe)$/Co-AMD pulse ratio. The number of cycles was 150, and the temperature in (a)–(d) and (f) 120 °C.

micrographs of a film deposited on Si which was structured with trenches of different sizes (obtained from an industry partner). High-resolution micrographs are shown for the narrowest trenches, which were 20 nm wide and 150 nm deep. It can be clearly seen that the coating is indeed very conformal with the ratio of the film thicknesses at the trench bottom and the top ranging between 0.8 and 1, highlighting the potential of our ALD process.

2.2. Crystallization

Samples with a 60 nm thick amorphous $PtCoO_2$ film were subjected to thermal treatments in different atmospheres. Annealing in Ar led to a phase separation and the formation of a Pt surface layer (Figures S8, S9, Supporting Information). In contrast, the delafossite $PtCoO_2$ phase could clearly be identified from grazing incidence XRD (GIXRD) patterns after annealing at temperatures between 700 and 800 °C in O_2 (**Figure 3**a). When the temperature was further increased to 900 °C, the films decomposed to CoO_x and Pt. These temperature transitions are similar to those reported for bulk $PtCoO_2$.[56]

A very surprising result was obtained when we tested the crystallization of much thinner films as these showed a strong (001) texture (Figure 3b). Therefore, we evaluated the films more extensively using TEM and (S)TEM (S = scanning). The micrograph of the ≈60 nm thick film in **Figure 4**a together with its Fourier transform in the inset confirms its polycrystalline nature without any apparent texture. In contrast, two-dimensional Pt planes nearly parallel to the surface are clearly visible in the high-angle annular dark-field (HAADF) STEM image in Figure 4c. Wei et al.[26] made similar observation in their solution-growth studies as they obtained strong (001) orientations for thin films but a loss of this orientation when thicker films were deposited. However, these researchers performed epitaxial growth on sapphire while the film in Figure 4c is grown on the amorphous native oxide of Si. A high anisotropy of the surface energy is the most likely explanation for this phenomenon. We want to highlight that such strongly oriented layers are quite rare for ALD-grown films.

To investigate the in-plane structure of the thin $PtCoO_2$ films, we deposited ≈10 nm $PtCoO_2$ on an amorphous SiN_x membrane and annealed the sample at 700 °C in O_2. Figure 4b shows an overview HAADF STEM image of such a film. The grain structure is readily visible with a pronounced bright spot

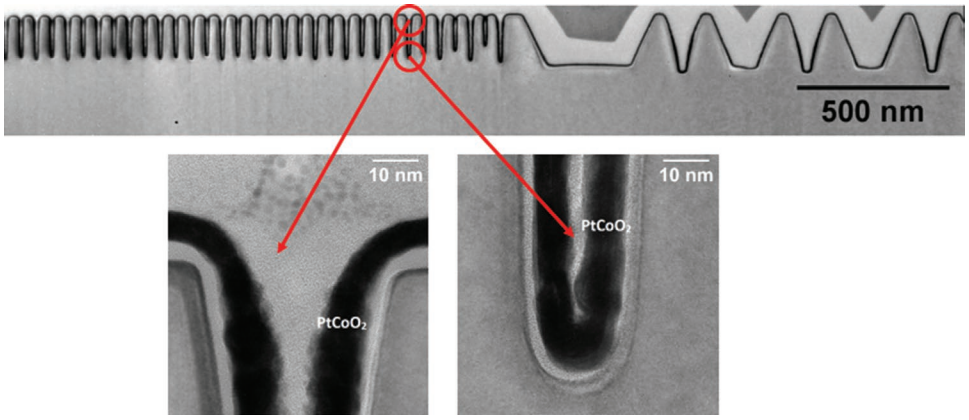

Figure 2. TEM micrographs of patterned Si sample coated with $PtCoO_2$.

in the middle of each grain as the grain nucleation point and small holes in black at the grain borders. The mean grain size is about 1 µm. Similar grain sizes were also observed in atomic force microscopy (AFM) investigations (Figure S6, Supporting Information). Diffraction patterns from large sample areas show discrete rings confirming a strong (001) orientation but a distribution of in-plane rotated grains. On these samples, we performed dark-field TEM imaging to obtain crystal orientation maps. Figure S10a in Supporting Information shows an orientation map constructed from three dark-field images with the respective diffraction-plane aperture positions indicated in the diffraction ring on the right. Due to the hexagonal symmetry of the diffraction pattern, the indicated aperture positions cover the complete set of orientations. Also, the area of a single aperture covers a range of diffraction spots originating from different neighboring orientation angles, thus, a single color in the orientation map indicates a certain set of orientations. Nevertheless, we find a distribution of single-crystalline grains with a typical size on the order of 1 µm. We checked this by recording selected-area diffraction patterns using an image-plane aperture selecting areas of 0.7 µm diameter often resulting in very narrow angular distributions of the diffraction patterns indicating a strain in the single crystals (Figure S10b, Supporting Information).

Next, we explored the possibility of epitaxial growth using (0001) sapphire substrates. As can be seen in Figure 3b the pattern of the Bragg-Brentano scan of the film on sapphire is similar to that on silicon indicating highly relaxed growth.

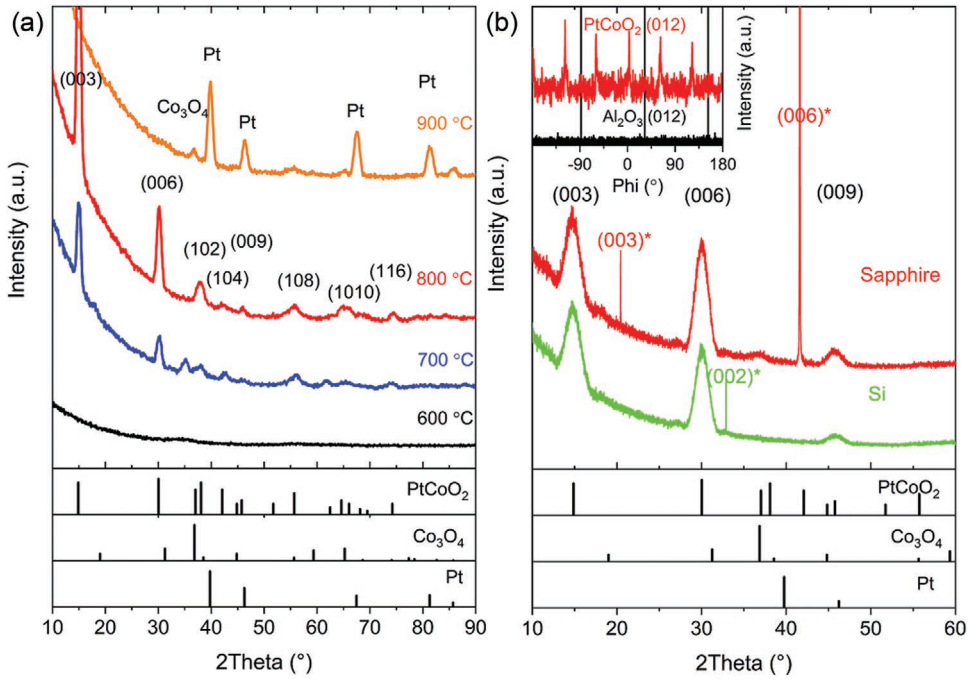

Figure 3. XRD analysis of $PtCoO_2$ films; a) GIXRD of ≈60 nm thick film annealed in O_2 at different temperatures, b) scans in Bragg-Brentano geometry of ≈5 nm thick films deposited on Si and sapphire and annealed at 700 °C. Asterisks denote substrate diffractions. The inset in (b) shows a phi scan on the (012) diffraction peak for the film on sapphire. (PDF cards: 00-027-1339, 00-042-1467, 00-004-0802).

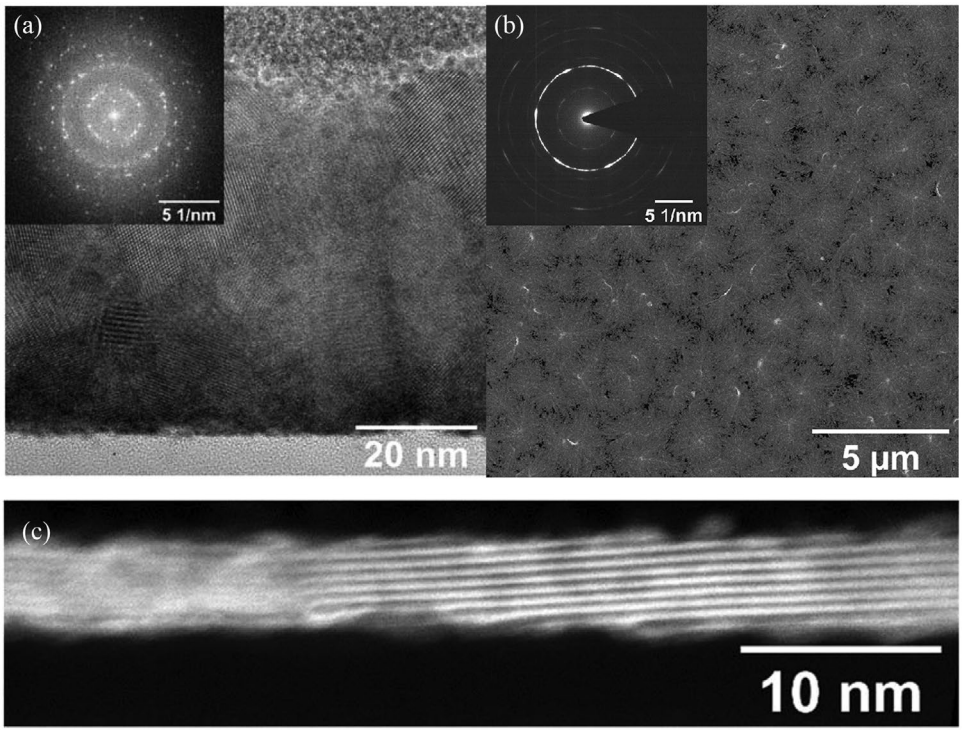

Figure 4. TEM investigations of $PtCoO_2$ films: a) cross-sectional micrograph of a ≈60 nm thick film, the inset shows the corresponding FFT pattern; b) top-view HAADF STEM micrograph of ≈10 nm thick film on a SiN_x membrane. The inset shows the electron diffraction pattern of the same sample; (b) cross-sectional HAADF STEM micrograph of a ≈5 nm thick film. The samples were annealed at 700 °C.

There is a small additional peak at 36.8°, which can be from $PtCoO_2$ (101) or Co_3O_4 contamination. The in-plane relationship between the sapphire substrate and the $PtCoO_2$ film was explored with a phi scan on the (012) diffraction. The $PtCoO_2$ film shows diffraction peaks at distances −30° and 30° from the substrate peaks, which is similar to the observations by Wei et al.[26] for solution processed films which indicates the coexistence of two epitaxial grain configurations, triangle, and inverted triangle.

The crystallization is accompanied by change of the chemical environment of the Pt cations as can be seen from the XPS investigation in Figure S3b, Supporting Information. The signals arising from Pt(I) become dominant, although small contributions from higher oxidation states are still present.

2.3. Electrical Characterization

The interest in $PtCoO_2$ is largely due to its excellent electrical properties.[16,15] Therefore, we measured the temperature-dependent electrical resistivity of a 10 nm thick $PtCoO_2$ film annealed at 700, 750, and 800 °C using the van-der-Pauw configuration (**Figure 5**a). The room-temperature resistivity values increase with increasing annealing temperature from 35 to 60 µΩcm; thus, they are one order of magnitude higher than the values reported for bulk single-crystals. The resistivity decreases with decreasing temperature as it is expected for metallic conduction, although the residual resistivity is quite high with residual resistivity ratios (RRR) ρ_{300K}/ρ_{15K} of about 1.3. An interesting detail is a slight increase of resistivity below 5 K. Kushwaha et al.[15] observed a similar increase at low temperatures but were not able to interpret it as they ruled out possible explanations such as the Kondo effect. The reasons for the high resistivity can be the polycrystalline nature of the film and the resulting grain-boundary scattering and the small deviation from the surface parallelism of the Pt sheets which can be seen from the STEM micrograph in Figure 4b. This limits the channel that electrons can move within the two-dimensional layers to dimensions smaller than the electron mean free path reported for single-crystalline $PtCoO_2$ (about 20 µm at low temperatures).[16]

In addition, Nandi et al.[16] reported a significant magnetoresistance for their $PtCoO_2$ crystals. For the comparison, we also performed temperature-dependent electrical resistivity measurements in the presence of an out-of-plane magnetic field with a magnitude of 9 T. As can be seen in Figure 5a, however, there is no indication for a similar field dependence of the resistivity. This might be explained by the reduced conductivity as the magneto-resistance is usually associated with high charge-carrier mobilities.[57]

Another unusual observation by Nandi et al.[16] was the presence of two different regimes of the Hall resistivity at high and low fields for temperatures in the range of 50 to 200 K. However, we did not make similar observations in our Hall measurements but observed a linear slope of the Hall resistivity in response to an applied field ranging from −9 to 9 T (Figure S11, Supporting Information). Therefore, we used a simple single-carrier-type model to calculate the electron density n_e. As can be seen in Figure 5b, n_e is about 2×10^{28} m^{-3} which is on the order of magnitude for typical metallic

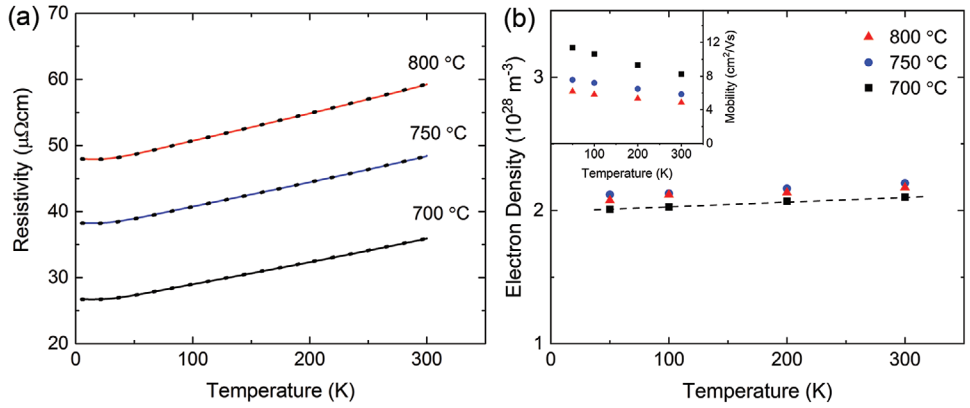

Figure 5. Electrical characterization of 10.27 nm thick $PtCoO_2$ film grown at 100 °C and annealed at different temperatures: a) resistivity versus temperature: the straight lines correspond to measurements without a magnetic field and the dots to measurements with a field of 9 T perpendicular to the sample surface; b) electron density at various temperatures determined from Hall measurements: the inset shows the corresponding mobility values calculated with the resistivity values from (a).

systems. Furthermore, n_e differs very little on the annealing temperature and shows only a weak temperature dependence. Combining the results from the resistivity and the Hall measurements, we calculated the electron mobilities μ_e (inset Figure 5b). For the film that was annealed at 700 °C, μ_e increases from about 8 cm^2 Vs^{-1} at room temperature to 12 cm^2 Vs^{-1} at 50 K. The μ_e values for the films annealed at 750 and 800 °C are slightly lower.

2.4. Exploration of Spintronic Properties

A large part of the spintronic devices, which are eagerly investigated at the moment, relies on the interaction between thin films of a magnetic material and a conductor that exhibits strong spin-orbit coupling (SOC). Here, the SOC can be responsible for the generation of spin currents via the spin Hall effect and the stabilization of certain spin textures in the magnetic layer via interfacial effects such as Dzyaloshinskii–Moriya interaction (DMI). Containing the 5d element Pt, the SOC in $PtCoO_2$ is considerably large, and its role in the formation of a single-band Fermi surface was demonstrated by Kushwaha and coworkers for example.[15] Moreover, a theoretical work by Kitamura et al.[17] indicated that the material shows a strong spin-Hall effect, although an experimental verification has thus far been obstructed by the difficulties of preparing thin-film structures suitable for typical experiments such as ferromagnetic-resonance measurements. In this work, we prepared two types of heterostructures: a multilayer consisting of 0.3 nm Co, 0.7 nm Ni, 0.3 nm Co and 3 nm TaN was deposited by magnetron sputtering on top of a 5 nm thick $PtCoO_2$ film, which had been annealed at 700 °C, and ≈10 nm $PtCoO_2$ was deposited on (111)-oriented yttrium iron garnet ($Y_3Fe_5O_{12}$, YIG), a ferrimagnetic insulator. The metallic multilayer is similar to magnetic layers regularly applied, e.g., by our group, for the fabrication of SOT-driven racetrack memories.[18,21,22,58,59] Here, the spin-injection layer has typically been a regular heavy metal such as Pt, Ir, or W. It is important to note the magnetic texture and therefore the functionality of these structures is extremely sensitive to details of the films including texture and interface sharpness. For example, perpendicular magnetic anisotropy (PMA) is readily induced by the growth on a strongly (111) textured Pt layer by interfacial magnetocrystalline effects.[18,60–62] Magnetic insulators such as YIG have attracted interest because spin can be transferred over wide distances such as a few μm via magnons.[63–66]

Figure 6a shows magnetic hysteresis curves of the $PtCoO_2$/Co/Ni/Co/TaN film stack measured at room temperature with

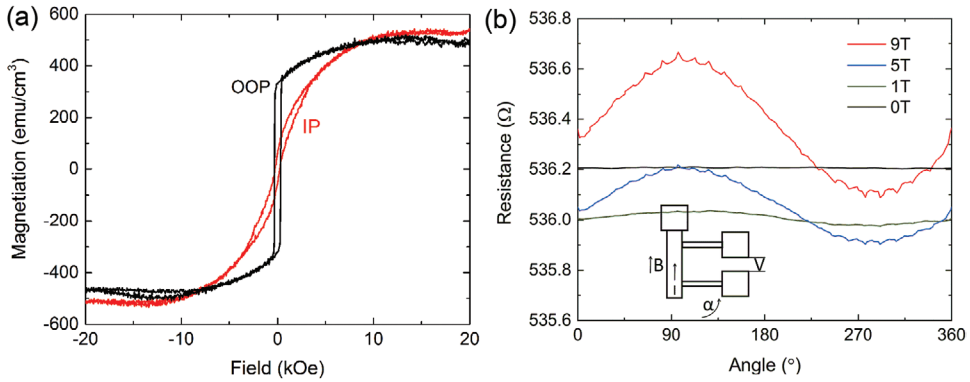

Figure 6. Analysis of the interaction of $PtCoO_2$ with magnetic materials: a) magnetic hysteresis loops of Co/Ni/Co multilayer deposited on a $PtCoO_2$ film; b) resistance of $PtCoO_2$ layer deposited on YIG under magnetic fields directed in varying angles α toward the current-flow direction.

the magnetic field applied parallel (in-plane, IP) as well as perpendicular (out-of-plane, OOP) to the surface using vibrating sample magnetometry (VSM). The nearly rectangular shape around the origin with a coercive field of 0.33 kOe the OOP loop proofs a magnetic easy axis along the surface normal. Congruently, the IP curve is mainly S-shaped indicating a hard axis in the film plane. However, the magnetic loop shows a substantial coercive field. Thus, a small part of the film might exhibit in-plane anisotropy. This might be caused by small impurity phases such as Co_3O_4 or differing magnetocrystalline effects whether the $PtCoO_2$/Co interface consists of a Pt sheet or a Co–O_x layer. However, this demonstrates that the magnetocrystalline anisotropy of the interface of (001) oriented $PtCoO_2$ and Co can be sufficient to overcome the stray-field effect and enforce PMA.

Hall bars were fabricated in a $PtCoO_2$ film deposited on YIG and the electrical resistance was measured with magnetic fields applied under varying angles α to the current direction within the sample plane (Figure 6b). A sinus-like variation of the resistance with α and an increase of $\Delta R = R(\alpha)\text{-}R(0)$ with an increasing magnetic field can be clearly observed. Possible explanations for this include the presence of a spin Hall effect and the associated spin torque acting on the magnetic YIG layer via the injected spin current.[67]

3. Conclusions

The ALD of the ternary oxide $PtCoO_2$ was accomplished with $Me_3Pt(CpMe)$, Co-AMD, and O_2 plasma over a wide temperature window from 100–320 °C. The as-deposited amorphous films were converted into the delafossite phase via annealing in oxygen at temperatures between 700 and 800 °C, while annealing in an inert atmosphere caused a phase separation and the formation of a Pt surface layer. We showed with XRD and TEM that thin films exhibited a strong (001) texture and consisted of grains with a horizontal size of about 1 µm while thicker films were randomly oriented. The films showed metallic conduction, and the resistivity decreased with decreasing temperature.

The suitability of $PtCoO_2$ for spintronic applications was tested in two ways: the magnetic anisotropy was measured for a Co/Ni/Co trilayer deposited onto $PtCoO_2$ and the angle-dependent magnetoresistance was determined for a $PtCoO_2$ film deposited on the magnetic insulator YIG. In the former experiment, we observed a strong PMA as it is required for applications such as ferromagnetic racetracks while the second experiment provided indications for the presence of a significant spin Hall effect as the resistance showed a sine-like variation under rotation in an in-plane magnetic field. Finally, we demonstrated the conformal deposition into trenches with an aspect ratio of 7.5:1 (20 nm wide, 150 nm deep) highlighting the potential of our ALD process.

As this work demonstrates for the first time an ALD process for a ternary oxide containing a platinum-group metal, it opens the potential for the development of ALD processes for further materials of this group. This includes further delafossites, particularly those based on Pd, pyrochlores (e.g., of iridium), and perovskites such as strontium ruthenate and strontium iridate, which exhibit phenomena such as non-trivial topology and non-collinear antiferromagnetism.

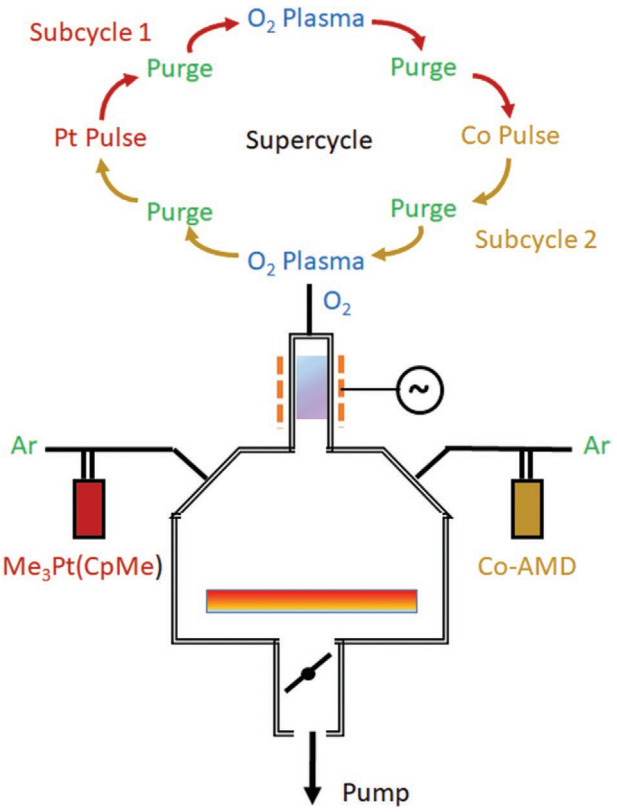

Figure 7. Illustration of the $PtCoO_2$ ALD process

4. Experimental Section

Film Growth: A schematic of the ALD experiments is depicted in **Figure 7**. The depositions were performed with an Oxford Instruments FlexAL reactor, which has a base pressure of about 1.5×10^{-6} Torr. Substrates were transferred via a load-lock. The working pressure during process steps can be controlled with a butterfly valve between 250 mTorr and about 10 mTorr under typical gas flow conditions. The reactor is equipped with a remote ICP source with a maximum power of 300 W which was used to generate O_2 plasma. The Co precursor Co-AMD was heated to 80 °C and the Pt precursor $Me_3PtCpMe$ to 40 °C. Both were stored in stainless steel bubblers, and Ar was used as carrier gas. Between the precursor and plasma exposures, the reactor was purged with N_2 and Ar. The ALD process consisted of the following sequence: [(Co-AMD pulse (t_{Co})–purge (5 s)–O_2-flow stabilization (4s)–O_2 plasma exposure (t_O)–purge (7 s))$_x$–($Me_3PtCpMe$ pulse (t_{Pt})–purge (5 s)–O_2-flow stabilization (4 s)–O_2 plasma exposure (t_O)–purge (5 s))$_y$]$_n$. The expressions in the parentheses are called subcycles and that in the square brackets is called a supercycle. In this work, $x = y = 1$ was considered except noted otherwise, and n was used to name the number of cycles. The ALD process was characterized by varying the substrate temperature (T_s), t_{Co}, t_{Pt}, t_O, the plasma power (P), and the pressure during the plasma exposure (p). While varying one parameter, the others were kept as follow: $T_s = 120$ °C, $t_{Co} = 3$ s, $t_{Pt} = 2$ s, $t_O = 15$ s, $P = 300$ W, and $p = 20$ mTorr. The number of supercycles was 150. Exceptions are noted in the text. For studying the formation of crystalline phases, films were annealed in a UniTemp RTP-100 oven using an O_2 or Ar atmosphere at temperatures ranging from 300 to 900 °C.

Characterization: The film composition was determined by XPS using a Thermofisher K-alpha spectrometer equipped with an Al source. Depth profiles were obtained by sputtering with Ar using an energy of 500 eV and the "low-current" mode. XRD in Bragg-Brentano as well as in grazing-incidence geometry was carried out in a Bruker D8 DISCOVER diffractometer for the determination of crystalline phases. The same tool was also used for X-ray reflection (XRR) to confirm the thickness measurements conducted with spectrometric ellipsometry (J. A. Woollam ESM 366). Furthermore, the morphology of the films was evaluated with AFM (Supporting Information).

The film properties were also investigated with (S)TEM. For this, cross-section samples were prepared by a focused ion beam lift-out route using a Tescan GAIA3 dual beam instrument. Plane-view samples were produced by growing the film directly on amorphous SiN_x membranes. Electron microscopy data was taken with a FEI Titan 80–300 (scanning) transmission electron microscope equipped with a CEOS CESCOR third-order axial geometric aberration corrector and a Gatan UltraScan 1000 slow-scan CCD camera. The primary electron energy was 300 keV. The homogeneous distribution of the constituents was checked by energy-dispersive X-ray spectroscopy (EDS) (supporting information).

Electrical and Magnetic Measurements: The temperature-dependent electrical resistivity was measured using a Quantum Design Dynacool 9T physical-property-measurement system (PPMS). The samples were cut to about 5×5 mm^2 sized squares and contacted in van-der-Pauw geometry by wire bonding. The currents were supplied by Keithley 6221 current sources, and the voltages were measured with Keithley 2182A nanovoltmeters. The measurements were controlled with a LabView program. The resistance values were recorded with increasing temperature for two comprehensive wiring geometries and the resistivity ρ was determined via

$$\rho = \frac{\pi d}{\ln 2} \frac{R_{AB,CD} + R_{BC,DA}}{2} f \quad (1)$$

where d is the film thickness, f is the geometry-dependent correction factor (for fairly to highly symmetric geometries close to unity) and $R_{AB,CD}$ is the resistance measured with the current applied through the contacts A and B and the voltage measured between the contacts C and D. The contacts are placed at the corners of the sample and numbered counterclockwise. $R_{BC,DA}$ has defined accordingly. The same instrumentation was also used to measure the Hall coefficient R_H at various temperatures, by cycling the magnetic field B between 9 and −9 T and measuring the voltage with an applied current $I = 100$ µA:

$$R_H = \frac{V_{DB,AC} + V_{AC,BD}}{2IB} d \quad (2)$$

where $V_{DB,AC}$ is the voltage measured between A and C with the current applied through the contacts D and B. From R_H, the charge carrier density n_e assuming only one type of carriers (electrons) is calculated:

$$n_e = \frac{1}{eR_H} \quad (3)$$

Here, e is the elemental charge. Finally, the electron mobility μ_e is obtained:

$$\mu_e = \frac{1}{en_e\rho} \quad (4)$$

In order to evaluate the potential of $PtCoO_2$ as spin-injection material for spintronic devices a Co/Ni/Co trilayer plus a TaN capping layer were deposited on a $PtCoO_2$-coated sample (annealed at 700 °C) using physical vapor deposition (PVD). The out-of-plane and in-plane magnetization was then measured with a Lake Shore Cryotronics 8600 Series vibrating-sample magnetometer (VSM). Furthermore, $PtCoO_2$ (10 nm, 120 °C, 3 s Co-AMD, 2 s $Me_3PtCpMe$, 15 s plasma, 20 mTorr) was deposited on YIG (200 nm on GGG, Matesy GmbH, Jena) and annealed at 720 °C. Hall bars with a length of 265 µm and a width of 80 µm were fabricated using laser maskless optical lithography and Ar-ion beam etching. The samples were contacted by wire bonding and placed in a PPMS with the surface parallel to the magnetic field. The resistance was then measured while rotating the sample around the axis perpendicular to the surface.

Supporting Information

Supporting Information is available from the Wiley Online Library or from the author.

Acknowledgements

The authors thank Dr. Hakan Deniz for his help with TEM measurements. Furthermore, the authors thank Dr. Kun-Rok Jeon for providing the YIG/GGG sample.

Open access funding enabled and organized by Projekt DEAL.

Conflict of Interest

The authors declare no conflict of interest.

Data Availability Statement

The data that support the findings of this study are available in the supplementary material of this article.

Keywords

ALD, atomic layer deposition, conductive oxides, delafossites, $PtCoO_2$ topological materials

Received: January 10, 2022
Revised: January 29, 2022
Published online: March 2, 2022

[1] X. Wan, A. M. Turner, A. Vishwanath, S. Y. Savrasov, *Phys. Rev. B* **2011**, *83*, 205101.
[2] S. M. Disseler, *Phys. Rev. B* **2014**, *89*, 140413(R).
[3] A. Juyal, A. Agarwal, S. Mukhopadhyay, *Phys. Rev. Lett.* **2018**, *120*, 096801.
[4] H. Kumar, K. C. Kharkwal, K. Kumar, K. Asokan, A. Banerjee, A. K. Pramanik, *Phys. Rev. B* **2020**, *101*, 064405.
[5] P. G. LaBarre, L. Dong, J. Trinh, T. Siegrist, A. P. Ramirez, *J. Phys.: Condens. Matter* **2019**, *32*, 02LT01.
[6] H. Liu, W. Tong, L. Ling, S. Zhang, R. Zhang, L. Zhang, L. Pi, C. Zhang, Y. Zhang, *Solid State Commun.* **2014**, *179*, 1.
[7] X. Liu, F. Wen, E. Karapetrova, J.-W. Kim, P. J. Ryan, J. W. Freeland, M. Terilli, T.-C. Wu, M. Kareev, J. Chakhalian, *Appl. Phys. Lett.* **2020**, *117*, 041903.
[8] K. Ueda, R. Kaneko, H. Ishizuka, J. Fujioka, N. Nagaosa, Y. Tokura, *Nat. Commun.* **2018**, *9*, 3032.
[9] W. K. Zhu, M. Wang, B. Seradjeh, F. Yang, S. X. Zhang, *Phys. Rev. B* **2014**, *90*, 054419.
[10] A. S. Patri, K. Hwang, H.-W. Lee, Y. B. Kim, *Sci. Rep.* **2018**, *8*, 8052.
[11] T. Nan, T. J. Anderson, J. Gibbons, K. Hwang, N. Campbell, H. Zhou, Y. Q. Dong, G. Y. Kim, D. F. Shao, T. R. Paudel, N. Reynolds, X. J. Wang, N. X. Sun, E. Y. Tsymbal, S. Y. Choi, M. S. Rzchowski, Y. B. Kim, D. C. Ralph, C. B. Eom, *Proc. Natl. Acad. Sci. USA* **2019**, *116*, 16186.
[12] M. Feigenson, J. W. Reiner, L. Klein, *Phys. Rev. Lett.* **2007**, *98*, 247204.
[13] L. Klein, Y. Kats, A. F. Marshall, J. W. Reiner, T. H. Geballe, M. R. Beasley, A. Kapitulnik, *J. Magn. Magn. Mater.* **2001**, *226*, 780.

[14] D. Roy, S. Davidovitch, Y.-M. Hung, M. Schultz, S. D. Albright, M. D. Morales-Acosta, F. J. Walker, J. W. Reiner, C. H. Ahn, A. D. Kent, L. Klein, *Phys. Rev. B* **2017**, 95.
[15] P. Kushwaha, V. Sunko, P. J. W. Moll, L. Bawden, J. M. Riley, N. Nandi, H. Rosner, M. P. Schmidt, F. Arnold, E. Hassinger, T. K. Kim, M. Hoesch, A. P. Mackenzie, P. D. C. King, *Sci. Adv.* **2015**, *1*, e1500692.
[16] N. Nandi, T. Scaffidi, P. Kushwaha, S. Khim, M. E. Barber, V. Sunko, F. Mazzola, P. D. C. King, H. Rosner, P. J. W. Moll, M. König, J. E. Moore, S. Hartnoll, A. P. Mackenzie, *npj Quantum Mater.* **2018**, *3*, 66.
[17] S. Kitamura, H. Usui, R.-J. Slager, A. Bouhon, V. Sunko, H. Rosner, P. D. C. King, J. Orenstein, R. Moessner, A. P. Mackenzie, K. Kuroki, T. Oka, (Preprint) arXiv:1811.03105, submitted Sept. **2018**.
[18] S.-H. Yang, S. Parkin, *J. Phys.: Condens. Matter* **2017**, *29*, 303001.
[19] W. Zhang, W. Han, X. Jiang, S.-H. Yang, S. S. P. Parkin, *Nat. Phys.* **2015**, *11*, 496.
[20] K.-S. Ryu, S.-H. Yang, S. Parkin, *New J. Phys.* **2016**, *18*, 053027.
[21] K.-S. Ryu, S.-H. Yang, L. Thomas, S. S. P. Parkin, *Nat. Commun.* **2014**, *5*, 3910.
[22] K.-S. Ryu, S.-H. Yang, L. Thomas, S. Parkin, *IEEE Trans. Magn.* **2016**, *52*, 1400404.
[23] T. Harada, K. Fujiwara, A. Tsukazaki, *APL Mater.* **2018**, *6*, 046107.
[24] P. Yordanov, W. Sigle, P. Kaya, M. E. Gruner, R. Pentcheva, B. Keimer, H.-U. Habermeier, *Phys. Rev. Mater.* **2019**, *3*, 085403.
[25] M. Brahlek, G. Rimal, J. M. Ok, D. Mukherjee, A. R. Mazza, Q. Lu, H. N. Lee, T. Z. Ward, R. R. Unocic, G. Eres, S. Oh, *Phys. Rev. Mater.* **2019**, *3*, 093401.
[26] R. Wei, P. Gong, M. Zhao, H. Tong, X. Tang, L. Hu, J. Yang, W. Song, X. Zhu, Y. Sun, *Adv. Funct. Mater.* **2020**, *30*, 2002375.
[27] E. Ahvenniemi, M. Matvejeff, M. Karppinen, *Dalton Trans.* **2015**, *44*, 8001.
[28] D. J. Hagen, T. S. Tripathi, M. Karppinen, *Dalton Trans.* **2017**, *46*, 4796.
[29] D. J. Hagen, M. Karppinen, *J. Vac. Sci. Technol., A* **2020**, *38*, 032412.
[30] J. Lybeck, M. Valkeapää, S. Shibasaki, I. Terasaki, H. Yamauchi, M. Karppinen, *Chem. Mater.* **2010**, *22*, 5900.
[31] T. S. Tripathi, J.-P. Niemelä, M. Karppinen, *J. Mater. Chem. C* **2015**, *3*, 8364.
[32] K. Uusi-Esko, E.-L. Rautama, M. Laitinen, T. Sajavaara, M. Karppinen, *Chem. Mater.* **2010**, *22*, 6297.
[33] M. Vehkamäki, T. Hatanpää, T. Hänninen, M. Ritala, M. Leskelä, *Electrochem. Solid-State Lett.* **1999**, *2*, 504.
[34] M. Vehkamäki, T. Hatanpää, M. Ritala, M. Leskelä, *J. Mater. Chem.* **2004**, *14*, 3191.
[35] M. E. Donders, W. M. Arnoldbik, H. C. M. Knoops, W. M. M. Kessels, P. H. L. Notten, *J. Electrochem. Soc.* **2013**, *160*, A3066.
[36] T. Aaltonen, M. Alnes, O. N. L. Costelle, H. Fjellvåg, *J. Mater. Chem.* **2010**, *20*, 2877.
[37] P.-A. Hansen, C. S. Granerød, Ø. Prytz, O. Nilsen, *J. Lumin.* **2019**, *215*, 116618.
[38] H. H. Sønsteby, H. Fjellvåg, O. Nilsen, *Adv. Mater. Interfaces* **2017**, *4*, 1600903.
[39] N. Labyedh, F. Mattelaer, C. Detavernier, P. M. Vereecken, *J. Mater. Chem., A* **2019**, *7*, 18996.
[40] Y. Wu, A. D. Giddings, M. A. Verheijen, B. Macco, T. J. Prosa, D. J. Larson, F. Roozeboom, W. M. M. Kessels, *Chem. Mater.* **2018**, *30*, 1209.
[41] A. J. M. Mackus, J. R. Schneider, C. MacIsaac, J. G. Baker, S. F. Bent, *Chem. Mater.* **2019**, *31*, 1142.
[42] T. Cheon, S.-H. Choi, S.-H. Kim, D.-H. Kang, *Electrochem. Solid-State Lett.* **2011**, *14*, D57.
[43] M. M. Minjauw, J.-Y. Feng, T. Sajavaara, C. Detavernier, J. Dendooven, *Dalton Trans.* **2022**, https://doi.org/10.1039/d1dt03543f.
[44] S.-W. Kim, S.-H. Kwon, D.-K. Kwak, S.-W. Kang, *J. Appl. Phys.* **2008**, *103*, 023517.
[45] J. Hämäläinen, F. Munnik, M. Ritala, M. Leskelä, *Chem. Mater.* **2008**, *20*, 6840.
[46] H. C. Knoops, A. Mackus, M. Donders, M. C. V. de Sanden, P. Notten, W. M. Kessels, *ECS Trans.* **2019**, *16*, 209.
[47] D. J. Hagen, M. E. Pemble, M. Karppinen, *Appl. Phys. Rev.* **2019**, *6*, 041309.
[48] M. E. Donders, H. C. M. Knoops, M. C. M. van de Sanden, W. M. M. Kessels, P. H. L. Notten, *J. Electrochem. Soc.* **2011**, *158*, G92 .
[49] K. B. Klepper, O. Nilsen, H. Fjellvåg, *Thin Solid Films* **2007**, *515*, 7772.
[50] K. B. Klepper, O. Nilsen, H. Fjellvåg, *J. Cryst. Growth* **2007**, *307*, 457.
[51] J. Kim, T. Iivonen, J. Hämäläinen, M. Kemell, K. Meinander, K. Mizohata, L. Wang, J. Räisänen, R. Beranek, M. Leskelä, A. Devi, *Chem. Mater.* **2017**, *29*, 5796.
[52] H. Zhang, D. J. Hagen, X. Li, A. Graff, F. Heyroth, B. Fuhrmann, I. Kostanovskiy, S. L. Schweizer, F. Caddeo, A. W. Maijenburg, S. Parkin, R. B. Wehrspohn, *Angew. Chem., Int. Ed.* **2020**, *59*, 17172.
[53] H. B. Profijt, P. Kudlacek, M. C. M. van de Sanden, W. M. M. Kessels, *J. Electrochem. Soc.* **2011**, *158*, G88.
[54] H. B. Profijt, W. M. M. Kessels, *ECS Trans.* **2013**, *50*, 23.
[55] P. F. Carcia, R. D. Shannon, P. E. Bierstedt, R. B. Flippen, *J. Electrochem. Soc.* **1980**, *127*, 1974.
[56] R. D. Shannon, D. B. Rogers, C. T. Prewitt, *Inorg. Chem.* **1971**, *10*, 713.
[57] M. N. Ali, J. Xiong, S. Flynn, J. Tao, Q. D. Gibson, L. M. Schoop, T. Liang, N. Haldolaarachchige, M. Hirschberger, N. P. Ong, R. J. Cava, *Nature* **2014**, *514*, 205.
[58] C. Garg, S.-H. Yang, T. Phung, A. Pushp, S. S. P. Parkin, *Sci. Adv.* **2017**, *3*, e1602804.
[59] Y. Guan, X. Zhou, F. Li, T. Ma, S.-H. Yang, S. S. P. Parkin, *Nat. Commun.* **2021**, *12*, 5002.
[60] Z. Luo, T. P. Dao, A. Hrabec, J. Vijayakumar, A. Kleibert, M. Baumgartner, E. Kirk, J. Cui, T. Savchenko, G. Krishnaswamy, L. J. Heyderman, P. Gambardella, *Sci.* **2019**, *363*, 1435.
[61] Z. Luo, A. Hrabec, T. P. Dao, G. Sala, S. Finizio, J. Feng, S. Mayr, J. Raabe, P. Gambardella, L. J. Heyderman, *Nature* **2020**, *579*, 214.
[62] M. Ota, M. Itou, Y. Sakurai, A. Koizumi, H. Sakurai, *Appl. Phys. Lett.* **2010**, *96*, 152505.
[63] Y. Kajiwara, K. Harii, S. Takahashi, J. Ohe, K. Uchida, M. Mizuguchi, H. Umezawa, H. Kawai, K. Ando, K. Takanashi, S. Maekawa, E. Saitoh, *Nature* **2010**, *464*, 262.
[64] S. Pütter, S. Geprägs, R. Schlitz, M. Althammer, A. Erb, R. Gross, S. T. B. Goennenwein, *Appl. Phys. Lett.* **2017**, *110*, 012403.
[65] K.-R. Jeon, J.-C. Jeon, X. Zhou, A. Migliorini, J. Yoon, S. S. P. Parkin, *ACS Nano* **2020**, *14*, 15874.
[66] M. B. Jungfleisch, V. Lauer, R. Neb, A. V. Chumak, B. Hillebrands, *Appl. Phys. Lett.* **2013**, *103*, 022411.
[67] R. Schlitz, A. A. Amusan, M. Lammel, S. Schlicht, T. Tynell, J. Bachmann, G. Woltersdorf, K. Nielsch, S. T. B. Goennenwein, A. Thomas, *Appl. Phys. Lett.* **2018**, *112*, 242403.